Tensile behaviour of glass FRCM systems with fabrics' overlap: Experimental results and numerical modeling

TENSILE BEHAVIOUR OF GLASS FRCM SYSTEMS WITH FABRICS' OVERLAP: EXPERIMENTAL RESULTS AND NUMERICAL MODELING

Jacopo Donnini[1], Gianluca Chiappini[2], Giovanni Lancioni[3], Valeria Corinaldesi[4]

[1] Dipartimento SIMAU, Università Politecnica delle Marche, Ancona, Italy, j.donnini@univpm.it

[2] Dipartimento DIISM, Università Politecnica delle Marche, Ancona, Italy, g.chiappini@univpm.it

[3] Dipartimento DICEA, Università Politecnica delle Marche, Ancona, Italy, g.lancioni@univpm.it

[4] Dipartimento SIMAU, Università Politecnica delle Marche, Ancona, Italy, v.corinaldesi@univpm.it

HIGHLIGHTS

- Tensile tests on glass FRCM systems with different fabrics' overlap lengths have been performed.
- DIC has been successfully employed to provide the FRCM strain field.
- A variational model has been numerically implemented to simulate the FRCM tensile behaviour.

ABSTRACT

The use of Fabric Reinforced Cementitious Matrix (FRCM) systems to reinforce existing masonry and concrete structures is nowadays a well-established practice. The mechanical characterization of FRCM systems is of fundamental importance to define the correct parameters needed to design a strengthening intervention. However, some aspects regarding FRCM tensile behaviour need to be further investigated.

The aim of this paper is to provide a detailed overview on the mechanical behaviour of FRCM specimens subjected to tensile tests. In this context, the effect of fabrics' overlapping on the global behaviour of the system is extensively analyzed. Different sample's configurations have been studied: one reinforced with a single layer of bidirectional glass fabric and three others with different fabrics' overlap lengths, varying between 100 and 200 mm. Digital Image Correlation (DIC) has been also used to measure displacements in experimental testing.

A phase-field model, that accounts for brittle fracture of cementitious matrix and fabric reinforcement and possible slippage at the fabric-to-matrix interface, has been developed. The

variational formulation has been implemented in a finite element code to simulate the tensile behaviour of FRCM systems and the effects of using different fabrics' overlap lengths.

Keywords:

FRCM; strengthening; tensile behaviour; overlap; Digital Image Correlation; modeling.

1. Introduction

The use of composite materials, consisting of inorganic matrices reinforced with fabrics in the form of open mesh textiles (Fabric Reinforced Cementitious Matrix), externally applied to masonry walls or concrete elements, is nowadays considered an effective and compatible reinforcement solution. FRCM have considerable advantages if compared to more traditional strengthening systems (e.g. Fiber Reinforced Polymer (FRP) or steel plates), such as high strength-to-weight ratio, ease of installation, high compatibility with masonry or concrete substrates, applicability on wet surfaces, resistance to high temperatures and safety for operators during installation [1-5].

FRCM systems have been successfully employed for flexural and shear strengthening of concrete beams [6-12], to confine concrete columns [13-17] and as in-plane and out-of-plane reinforcement of masonry walls [18-23]. However, there are still no standardized procedures for the mechanical characterization of FRCM systems, and, to date, ACI549.4 R-13 is the only guideline that provides for the design of reinforcement interventions with these systems [24].

The tensile characterization of FRCM systems is usually carried out by means of two test setups, the clevis-grip method, required by ACI549.4 R-13 and described in AC434-13 [25], and the clamping-grip method, recommended by Rilem TC 232-TDT [26]. These two test methods provide for different boundary conditions at the specimens' ends and can lead to significantly different results [27,28]. Even if the mechanical characterization of FRCM systems has been investigated by several authors [27-30], with different techniques and different materials, there are still some aspects that need further investigation.

One that deserves attention is represented by the fabrics' overlap. The limited width of the rolls in which the fabric is provided by manufactories (about 1 meter), often causes the need to overlap the fabrics. The minimum overlap length between two fabrics, which should be defined for each FRCM system, guarantees the complete transfer of tensile stresses from one fabric to another. An overlap length greater than the minimum overlap length, should promote the failure of the FRCM reinforcement before debonding of the overlapped FRCM fabrics. Tensile tests on FRCM coupons with fabrics' overlap are required by AC434 [25] and the most recent Italian guideline issued by CSLP [31]. During FRCM installation, it is important to provide sufficient overlap when splicing fiber fabrics, as determined according to test methods specified in [25]. The required overlap, or lap-splice length, depends on the tensile strength and thickness of the FRCM material system and on the bond strength between adjacent layers of FRCM reinforcement [24].

In this study, the effects of different glass fabrics' overlap lengths on the mechanical behaviour of the composite material have been analyzed through tensile tests on prismatic coupons, and then a minimum overlap length related to the system analyzed has been identified. It is important to understand if the lap can cause the formation of a weak section with respect to the continuous fabric section. The objective is to determine the minimum fabrics' overlap length able to maintain fabric continuity and to avoid a loss of tensile strength in FRCM specimens.

Furthermore, in order to obtain the mechanical parameters needed for the strengthening design, it is also important to identify a reliable way to measure the deformations of FRCM systems during tensile tests. For this kind of material, consisting of both an inorganic matrix that cracks when subjected to tensile stresses and a fabric that can slip within the matrix, it may be difficult to measure displacements and deformations in an accurately way relying on traditional sensors. Strain gauges can measure only local values and do not allow to monitor the 'tension stiffening' effect of the mortar after the formation of cracks. As for LVDTs, the position of the instruments with respect to the cracking pattern, clearly unknown before the test, can affect the reliability of results.

The use of full-field contactless optical methods, such as Digital Image Correlation (DIC), could be a possible solution that does not interfere with the specimen during the test, and it is not affected by the formation of cracks on the specimen surface. This method has been already successfully applied by the authors in testing of metals [32], brittle materials such as ceramics [33], rubber [34], foam [35] and cork [36]. The application of DIC to FRCM systems has been investigated by Tekieli et al. [37] and Bilotta et al. [38]. In both cases DIC provided reliable results and additional information that would have been unavailable otherwise.

In this study, DIC has been successfully used to monitor the evolution of the strain field during tensile tests and has been able to provide important information about the evolution of the cracks pattern, local deformations and width of the cracks.

For a better comprehension of the experimental results, a damage model has been numerically implemented in a finite element code, and simulations have been performed to reproduce the FRCM tensile response. A phase-field approach has been followed to develop the model, according to which fracture is approximated by a smooth damage variable and governing and evolution equations are variationally deduced by minimizing proper energy functionals, depending on damage and its gradient [39]. In the last years, following the pioneering paper [40] (see [41] for a more detailed description), several variational formulations were proposed to reproduce many different failure modes (e.g., shear fracture [42], rupture due only to tensile loads [43,44], ductile failure [45]), and to describe failure of different materials (rubbers [46], cement mortar [47], fiber reinforced concretes [48], etc.). Variational approaches were also applied to plasticity in [49-51], and to coupled damage and plasticity in [52]. Applications of phase-filed models to FRCM systems were proposed in [53,54]. Debonding of fiber yarns was modeled in [53] by assuming that the damage energy of the yarn-to-matrix interface has the form of power functions, while, in [54], a specific damage dependent energy term was included in the interface energy, to account for frictional slippage.

In this paper, the model proposed in [55] for hybrid laminates, is revised and adapted to the specific problem of tensile FRCM systems. FRCM specimens are schematized as multilayer systems constituted by layers of mortar and reinforcement. Each layer is modeled as a brittle bar that elastically stretches and, when a limit stress is reached, it breaks. Its energy collects three contributions, as usually in phase field theories [39]: an elastic term, a local damage term and a non-local gradient part. Different stiffnesses and strengths have been assigned to the anchor parts and to the central free parts of mortar layers. Each layer is connected to the adjacent one by non-linear springs, which allow elastic shear strain and slippage in regime of stress softening. Balance and evolution equations are determined by energy minimization. Regarding the evolution, an incremental procedure is adopted, consisting in solving a constrained programming problem at each increment of the imposed tensile deformation. A similar evolution scheme was analytically solved in [48], in a simplified one-dimensional context, providing parametric and stability

analyses. Here the evolution problem is solved numerically, by implementing the model in a finite element code. Simulations are performed by considering specimens with a single reinforcement layer and with overlapped double reinforcement layers. All the evolution phases that leads to specimens' failure are accurately captured by simulations, whose predictions are in good agreement with the experimental evidences.

The paper is organized as follows: after a description of the materials used to manufacture FRCM coupons (Section 2) and of the tensile test setup adopted (Section 3), experimental results are reported in Section 4. In this section the effect of fabrics' overlapping on the mechanical behaviour of FRCM systems is analyzed. The possibility of using different measurement methods (DIC, displacement transducer and extensometer) is also discussed. Finally, a phase-field model has been developed (Section 5), in order to reproduce the tensile behaviour of FRCM coupons reinforced with single or overlapped layers of glass fabrics. Numerical results have been described in Section 6 and compared with those obtained in experiments.

2. Materials

A bidirectional fabric made of alkali resistant (AR) glass fibers coated with a layer of polyvinyl alcohol (PVA) was considered. The fabric structure is attained through leno wave technique, with weft yarns that pass through the warp yarns. Geometrical properties of the glass fabric employed are reported in Fig. 1.

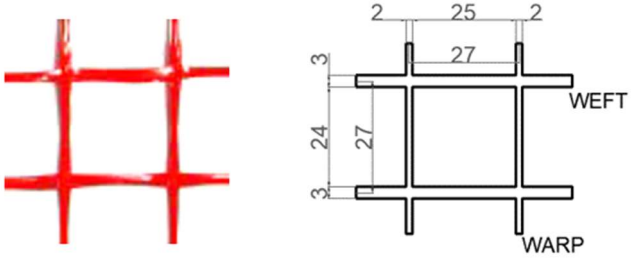

Fig. 1 – Geometrical properties of the glass fabric employed (250 g/m^2)

The mechanical properties of the glass fabric were determined through tensile tests on single fiber yarns taken from the warp direction. Tensile tests on glass fiber yarns were performed in displacement-control at a rate of 0.5 mm/min, by using a tensile testing machine with a load bearing capacity of 50 kN. Specimens comprised one fiber yarn 300 mm long. FRP tabs were epoxy-bonded to the ends of the specimen to ensure slip-free gripping by the testing machine. The cross-sectional area of the single yarn A_f (Table 1) was computed from the nominal thickness provided by the manufacturer. A macro extensometer with a length of 50 mm was positioned at the center of each specimen to measure the strain of the yarn. The mean tensile strength σ_f, the corresponding strain ε_f, and the elastic modulus E_f are obtained by averaging the results of 5 specimens and are reported in Table 1 together with the corresponding coefficient of variation, CoV.

A lime-based mortar was used as FRCM matrix. Three prismatic specimens (40x40x160 mm^3) were cast, cured at laboratory conditions (20 °C, 70% RH) up to 28 days and tested according to EN 1015-11 [56]. The average flexural strength $\sigma_{m,f}$, compressive strength $\sigma_{m,c}$ and elastic modulus

in compression E_m, are reported in Table 1 together with the corresponding Coefficient of Variation, CoV.

Table 1 – Mechanical properties of glass yarns (warp direction) and inorganic matrix

Material		σ_f [MPa]	ε_f [%]	E_f [GPa]	A_f [mm^2]	$\sigma_{m,f}$ [MPa]	$\sigma_{m,c}$ [MPa]	E_m [GPa]
Glass 250	Average	1405	2.4	57.1	0.923	-	-	-
	CoV	*0.102*	*0.061*	*0.087*	-	-	-	-
Matrix	Average	-	-	-	-	4.1	10.2	9.5
	CoV	-	-	-	-	*2.9*	*0.025*	-

3. Experimental investigation

3.1 Specimens preparation

FRCM coupons (dimensions of 70x400x10 mm^3) were manufactured by first applying a thin layer of mortar of about 5 mm, using a wooden formwork. A layer of glass fabric was then placed on top of the mortar and covered with a second layer of mortar with same thickness. Coupons were cured at laboratory ambient conditions at 20 °C and 70% relative humidity for 28 days. After that, four metal tabs were applied with epoxy at the ends of each specimen (Fig. 2) with an anchor length of 150 mm, as indicated in the AC434.
In addition to the one ply specimen (Fig. 3a), panels with a lap splice overlap of 100, 150 and 200 mm were manufactured, following the same procedure. Geometrical properties of FRCM specimens with fabrics' overlap are illustrated in Fig. 3b. The free length of the specimen (equal to the distance between the metal plates) has been varied according to the overlap length. The anchor length between metal plates and specimen has been kept constant (150 mm).

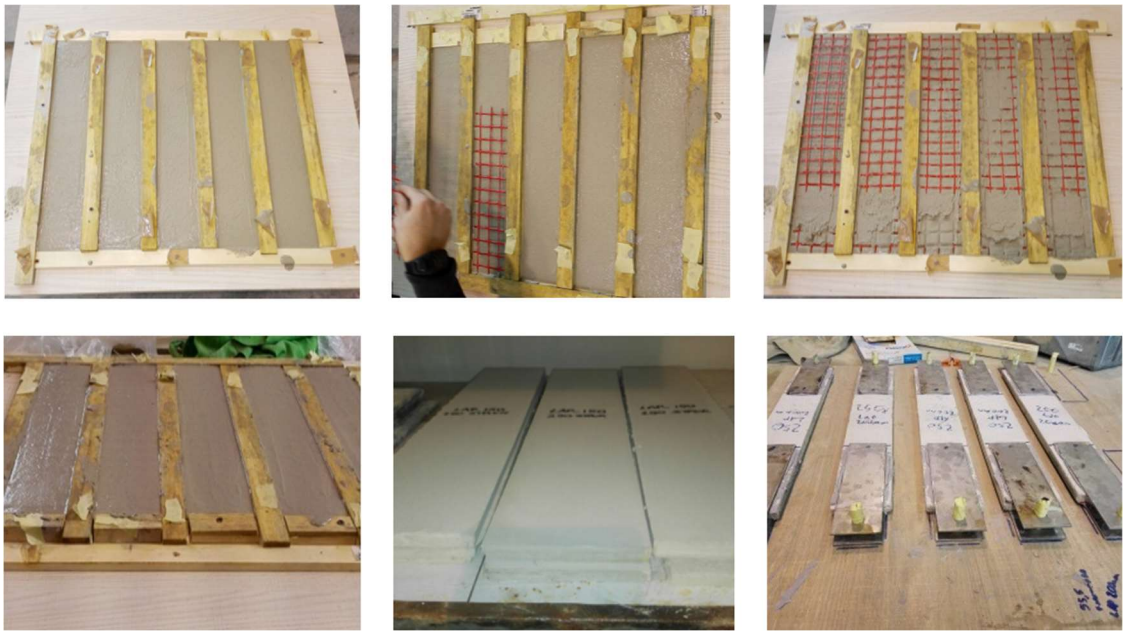

Fig. 2 – Preparation of FRCM coupons with fabrics' overlap

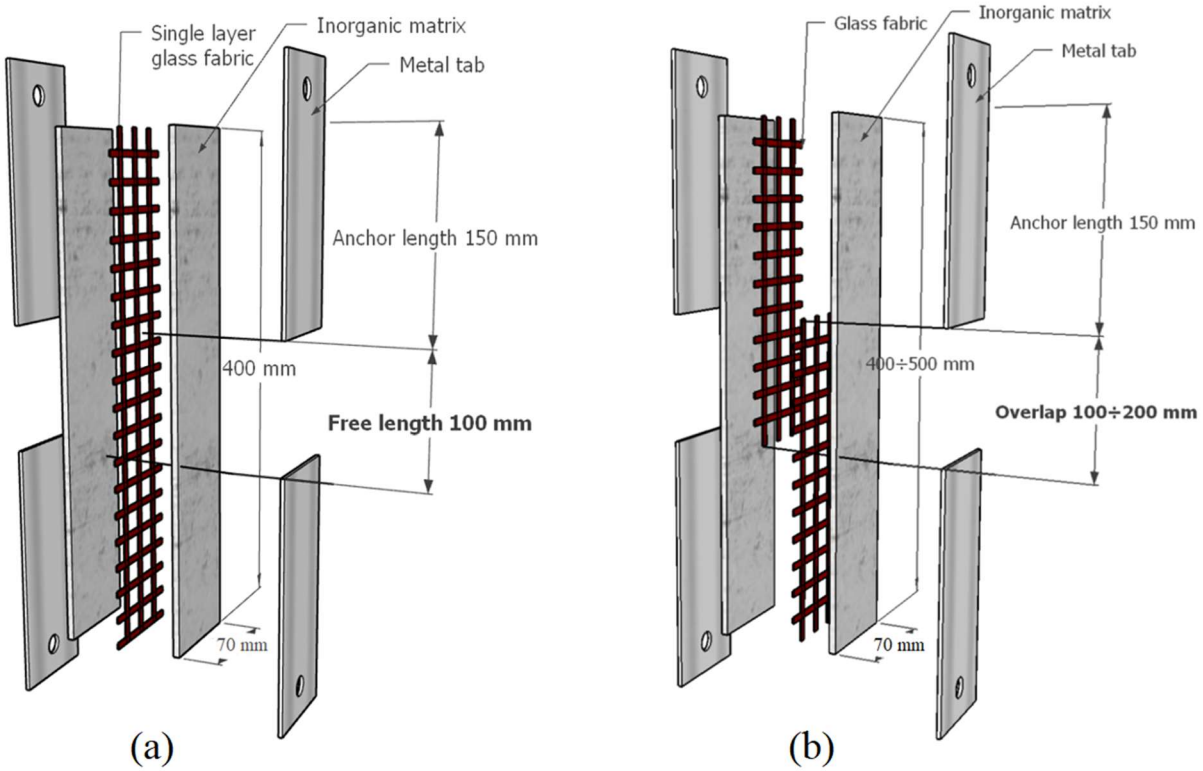

Fig. 3 - Geometrical properties of FRCM coupons with a single layer of glass fabric (a) and with fabrics' overlap (b).

3.2 Tensile Test Setup

A total of 20 specimens have been manufactured and tested using a clevis-type gripping system, as recommended by the US guideline AC434.13 Annex A, in which the load is transferred from the testing machine to the mortar by shear adhesion, using metal tabs directly bonded to the mortar surface. If compared to the test setup proposed by RILEM TC 232-TDT ("clamping grip" is the term used for load application through compressive stress normal to the specimen's plane), the system proposed by AC434 ("clevis grip") does not provide for the application of compressive forces at the specimen's ends, leaving the fabric free to slip within the mortar. This system is connected to the testing frame with a clevis joint (Fig. 4). Tests were conducted under displacement control at 0.5 mm/min by using a tensile machine with a load bearing capacity of 50 kN. The global displacement was recorded by the LVDT integrated in the testing machine, while the local axial deformation was measured using a clip-on extensometer with a 100 mm gauge length directly applied at the ends of the metal tabs (Fig. 4).

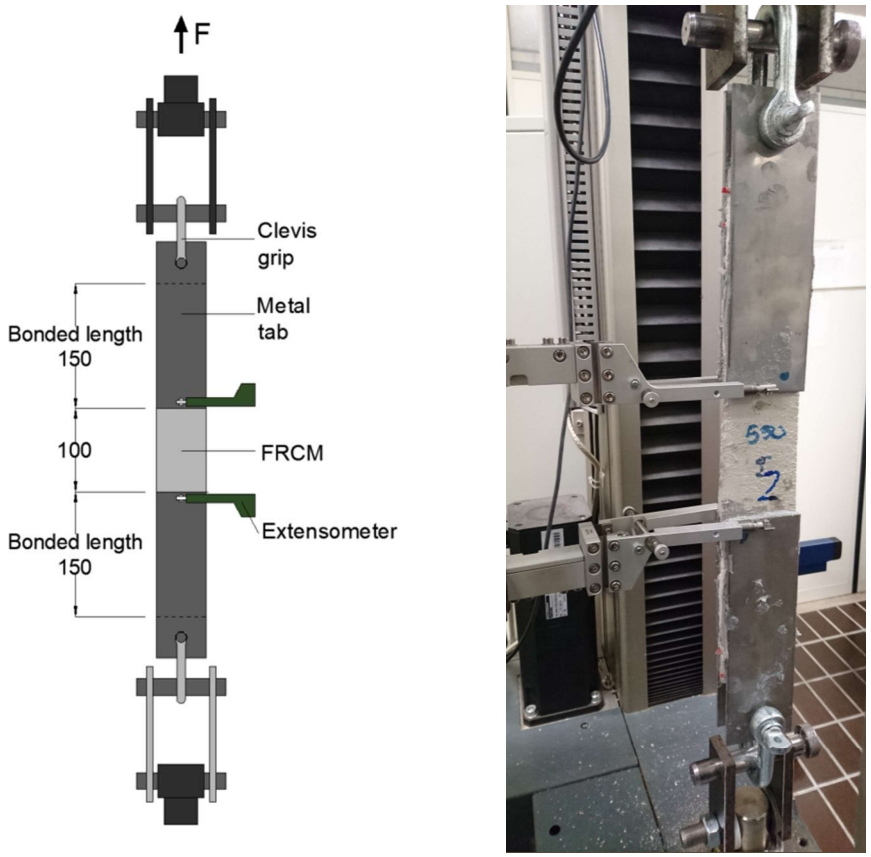

Fig. 4 – FRCM tensile test setup: strains measured with macro extensometer

3.3 Digital Image Correlation

Digital Image Correlatation (DIC) was also used as additional measurement system. DIC offers the possibility to monitor strains and displacements on the whole surface of the specimen and allows to select the area of the sample in which the strain field is required (in this case the area in between the metal tabs).
The main characteristics of experimental and DIC set-up are given in Table 2 and shown in Fig. 5.

Table 2 – Optical set-up and DIC characteristics

Sensor	[Type]	CMOS
Sensor pixel size	[µm]	6.8 × 6.8
Sensor resolution	[pixel]	1280 × 1024
Frame rate	[fps]	27
Lens	[Type, mm]	C mount, 16
Working distance	[mm]	≈ 800
Sensor noise	[gray level, dB]	0.94, −19
Subset size	[pixel, mm]	24, 3
Displ. accuracy (st. dev)	[pixel, mm]	±[0.01, 0.05]
Strain accuracy (st. dev)	[mm/mm]	±0.00022

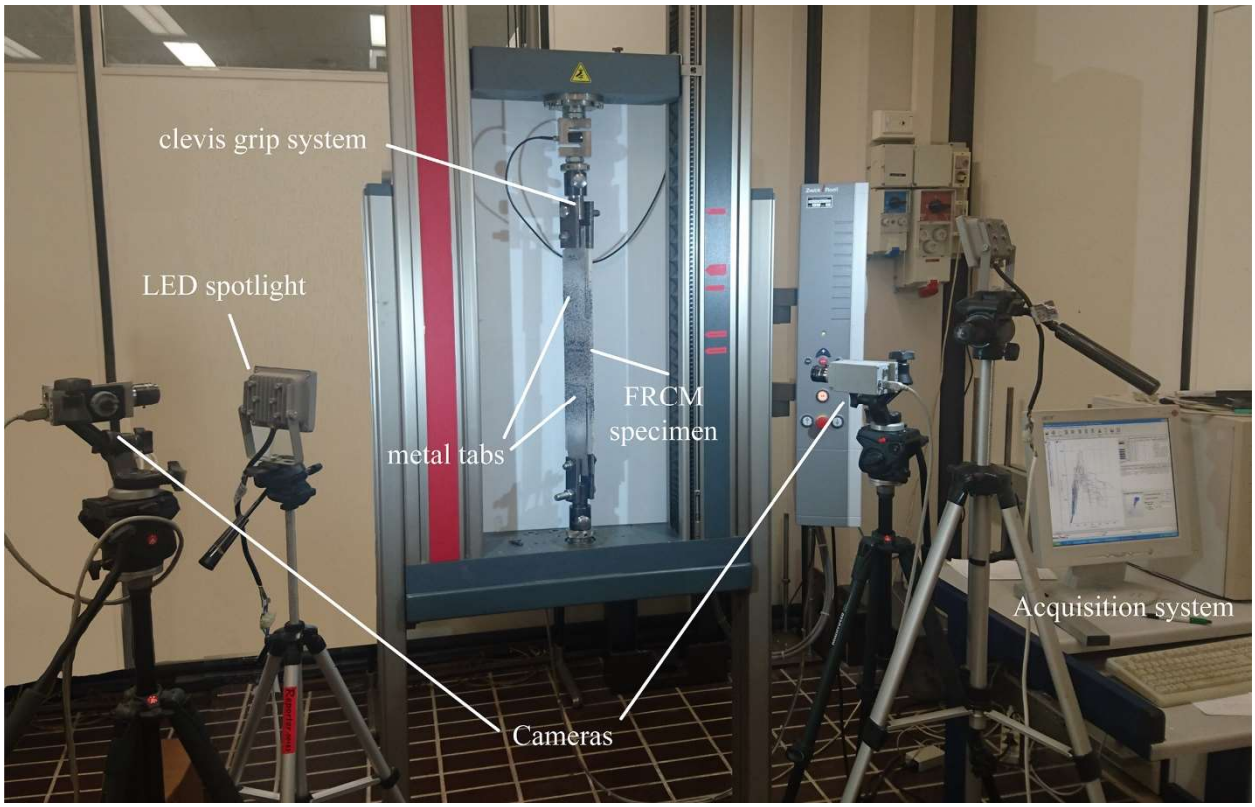

Fig. 5 – FRCM tensile test setup with Digital Image Correlation (DIC) acquisition system

During the tests, pictures of the frontal surface of the specimens have been acquired by a digital camera (model Pixelink® B371F - camera on the left in Fig. 5) at 2 frame per second, collecting about 600 images. The camera was equipped with a lens having a focal length of 16 mm and placed about 800 mm away from the specimen, in order to reduce the perspective errors due to eventual out-of-plane motions. The specimen was illuminated using an LED spotlight. A second camera, placed on the right side (camera on the right in Fig. 5), was used to monitor possible motions out of the plane.

A speckle pattern, consisting of black dots randomly distributed over the specimen surface, was firstly realized by means of spray painting. The size of the spots was chosen in relation to the size of the specimens and the position of the cameras. The pictures acquired during the tests have been post-processed by an in-house developed DIC software. The correlation method here adopted is based on global DIC, which incorporates the assembling approach of Finite Element method. A grid of points was drawn on the free surface of the specimen, in order to measure displacements and deformations over the free length of the specimen. Displacements of all nodes of the grid are obtained by minimizing the correlation error computed all over the current frame with respect to the reference frame [57]. The zero-mean sum of square difference (ZSSD) criterion was adopted to avoid the effects of lighting offset and inhomogeneity. A typical picture recorded by the camera and the grid drawn on the specimen, together with its histogram and strain noise evaluation are shown in Fig. 6.

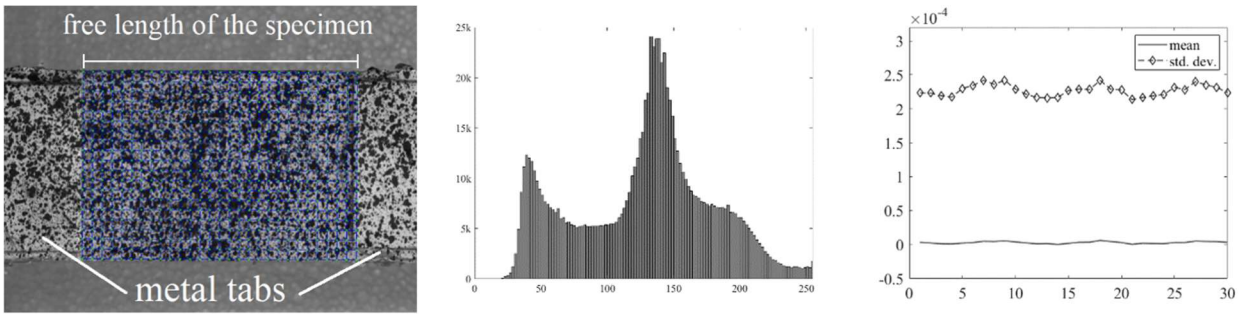

Fig. 6 – Grid (a), histogram (b), and strain noise evaluation for the DIC image (c)

The picture on the left (Fig. 6a) show the subsets discretization used for the image analysis: the subset size was typically 24×24 pixels that means a measure point about each 3 mm.
The strain used in the subsequent elaboration has been computed by means of the Cauchy-Green theory, within the framework of large displacements and large deformations, starting from the node displacements. The components of the Hencky strain tensor ε_x, ε_y, and ε_{xy} have been computed.
To assess the quality of the correlation technique and strain measurement, a set of 30 stationary images was acquired and analyzed before the test of the specimen; the average values of the strain distribution and its standard deviation within each frame are shown on Fig. 6b,c. No bias is observed since the average strains present small random oscillations around zero. The standard deviations are nearly constant, in the order of 220 με.
Strains reported in Table 3 ($\varepsilon_{u,DIC}$), and those of the experimental curves of Fig.7, were calculated by means of DIC. Global strain was calculated by measuring the mean strain over the free length of the specimen (Fig. 7a). By doing so, results obtained with the use of macro-extensometer (applied at the ends of the metal tabs) can be compared. A sequence of axial displacement and strain maps measured at different instants is reported in next section (Fig.8).

4. Experimental results

4.1 Tensile tests on glass FRCM systems

The results of tensile tests on glass FRCM systems in terms of stiffness modulus (E_u), ultimate stress (σ_u) and ultimate strain (ε_u), together with the failure mode observed and the corresponding coefficient of variation (CoV), are reported in Table 3.

Ultimate strain has been determined in different ways: by dividing the total displacement measured at the load cell for the total length of the specimen ($\varepsilon_{u,TOT}$), by means of an extensometer with gauge length of 100 mm directly applied at the ends of the metal plates ($\varepsilon_{u,Ext}$) and with the use of digital image correlation (DIC) technology ($\varepsilon_{u,DIC}$). In the case of specimens G-250_Lap150 and G-250_Lap200 the extensometer could not be used due to the distance between the metal plates exceeding 100 mm.

For the determination of the ultimate stress, the measured force (F) was divided by the cross-section of the textile reinforcement (A_f) in the load direction. The modulus of the cracked specimen (E_u) was calculated as the slope of the segment of the response curve between two points equal to 0.90 σ_u and 0.60 σ_u as indicated in the AC434.13.

Table 3 – Results of Tensile Tests [according to AC434, Annex A]

Specimen		F_{max} [kN]	σ_u [MPa]	$\varepsilon_{u,TOT}$	$\varepsilon_{u,Ext}$	$\varepsilon_{u,DIC}$	E_u [GPa]	Failure mode
G250	Average	3.53	1275	0.0139	0.049	0.047	28.92	F
	CoV	*0.059*	*0.059*	*0.125*	*0.218*	*0.112*	*0.129*	
G250_ Lap100	Average	2.16	780	0.0150	0.044	0.041	9.52	S
	CoV	*0.036*	*0.036*	*0.124*	*0.232*	*0.278*	0.243	
G250_ Lap150	Average	3.52	1270	0.0117	-	0.027	41.27	F
	CoV	*0.057*	*0.057*	*0.071*	-	*0.156*	*0.077*	
G250_ Lap200	Average	3.43	1239	0.0118	-	0.021	44.05	F
	CoV	*0.091*	*0.091*	*0.128*	-	*0.158*	*0.182*	

S) Slippage of the fabric within the matrix
F) Fabric breakage

Experimental stress-strain curves are reported in Fig.7, together with curves obtained from numerical simulations, which will be discussed in Section 6.

The first segment of the curve represents the uncracked state, where the composite properties depend on the matrix characteristics. The load drop after the formation of the first crack is mainly due to the modest fabric volume. After this phase, once the transfer of stress from the matrix to the fabric has occurred, the load starts to increase again, with an evident post-cracking hardening phase. This phase is mainly governed by the fabric properties and bond properties at the interface between fabric and mortar. The presence of 'jumps' on the second part of the stress-strain curve is due to the formation of further small cracks within the mortar, which however do not significantly affect the FRCM hardening behavior.

Results show that a fabrics' overlap length of 100 mm (G250_Lap100) is not enough to guarantee the complete transfer of tensile stresses from one fabric to another. Fabrics slip on each other and the maximum load reached is almost half of that obtained with a single fabric layer (G250).

Increasing the overlap length up to 150 mm allows to restore the specimen integrity and to reach an ultimate stress equal to that of the specimen with continuous fabric.

Longitudinal strains measured by extensometer ($\varepsilon_{u,Ext}$) and DIC ($\varepsilon_{u,DIC}$) of specimens G250 and G250_Lap100 are in good agreement, and thus demonstrate that the two measurement methods are reliable and both can be used.

Specimens with fabrics' overlap equal or greater than 150 mm showed higher stiffness with respect to specimens with continuous fabric (G250). The stiffness modulus of the cracked phase (E_u) for specimens G250_lap150 and G250_lap200 is about 45% greater than that of specimens G250. The higher stiffness is due to the presence of two layers of fabrics over the free length of the specimen. However, the failure of the specimens with fabrics' overlap always occurs for stress values equal or slightly lower to those of specimens with continuous fabric. This is due to the failure mode that always involves only one layer of fabric, at the end of the overlap and close to the metal tabs (see Fig. 8c,d).

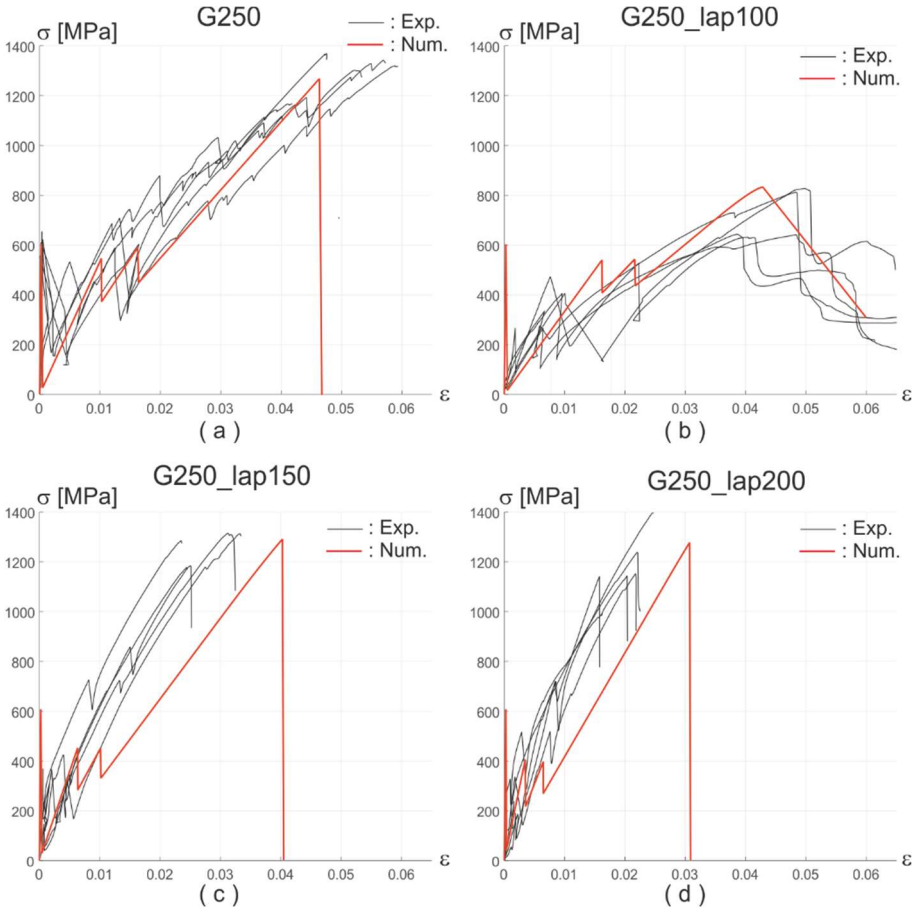

Fig. 7 – Experimental and numerical stress-strain curves of Glass-FRCM with a single fabric reinforcement layer (a), and two layers with a lap splice overlap of 100, 150 and 200 mm (b,c,d)

Displacement and strain fields over the free length of the FRCM and the evolution of cracks formation under increasing loads have been recorded by DIC and reported in Fig. 8. It can be clearly observed that maximum deformations are recorded in correspondence with the formation of two or three major cracks, which evolve as the load increases, while the portion of mortar between the cracks remains almost undeformed.

Strain peaks are smaller for specimens with fabrics' overlap length of 150 and 200 mm, thus indicating the formation of smaller cracks within the mortar.

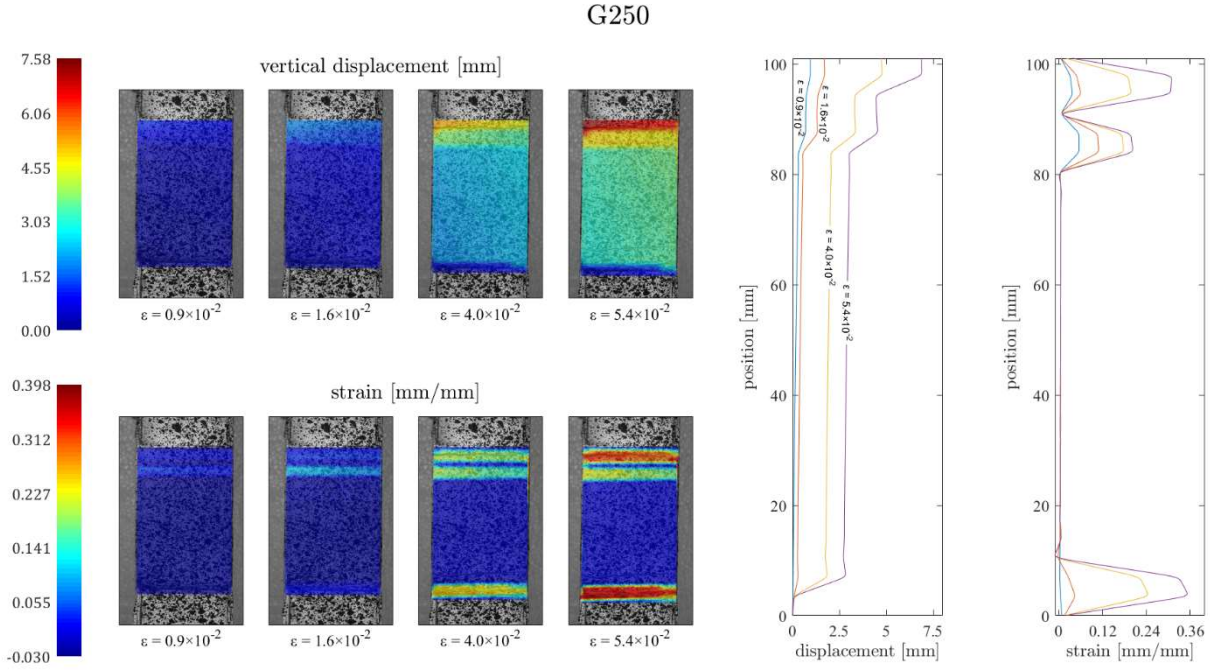

(a)

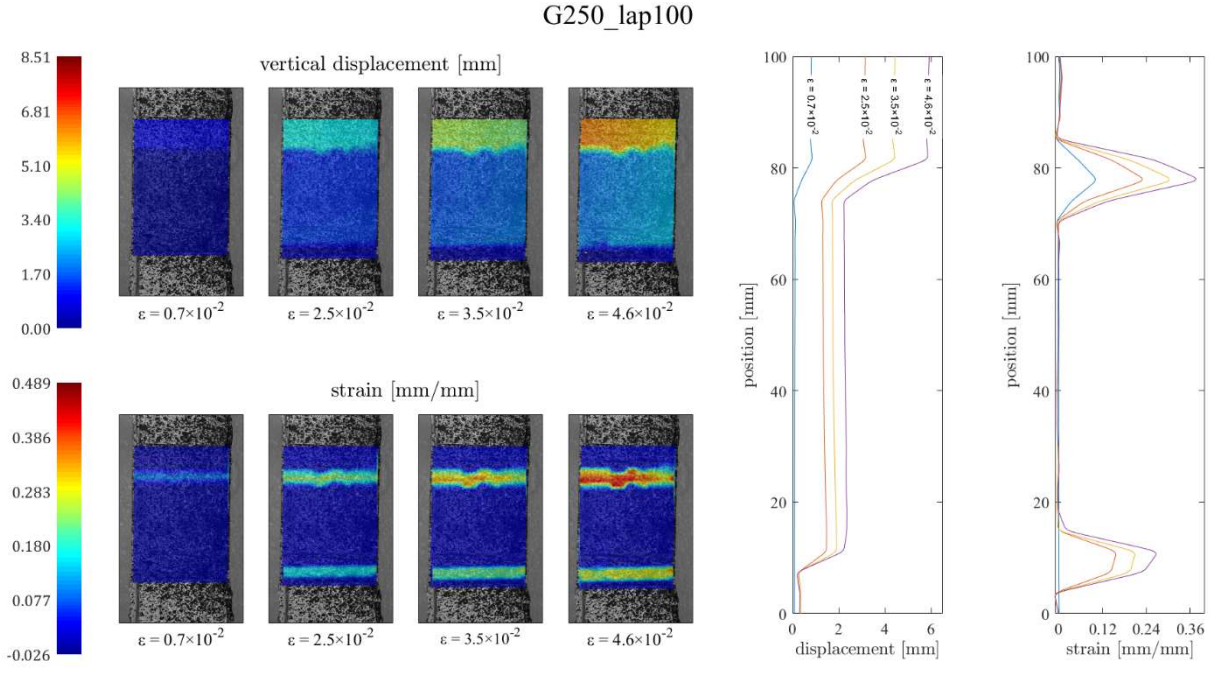

(b)

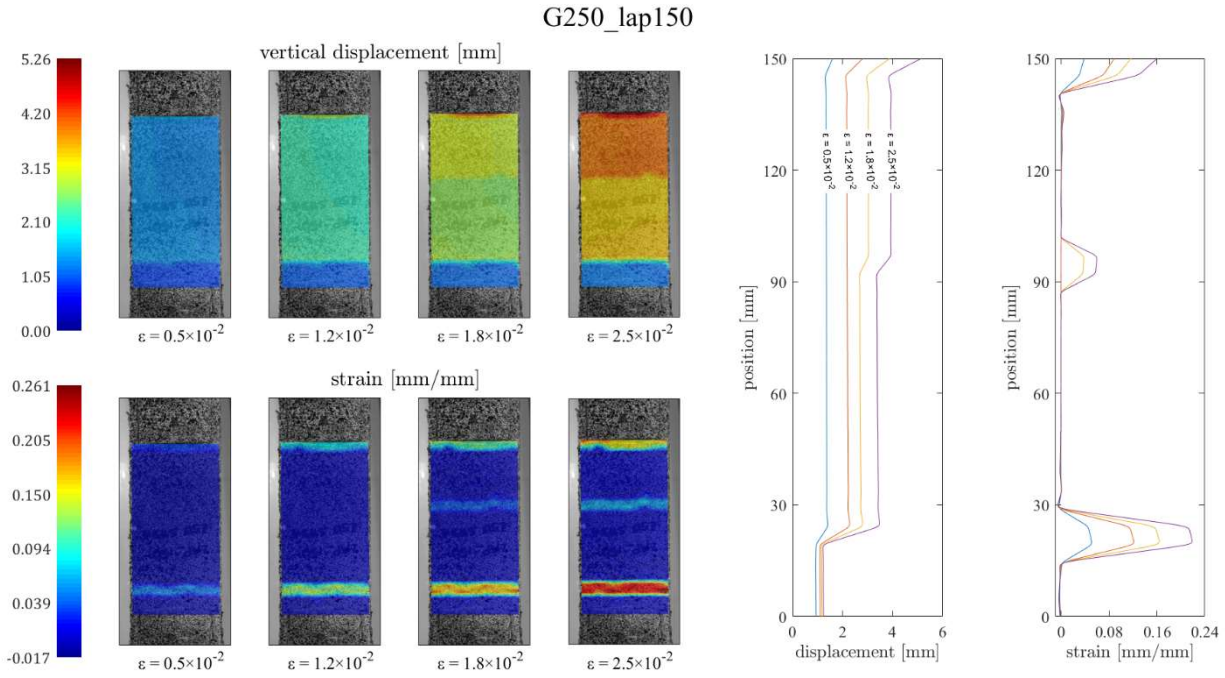

(c)

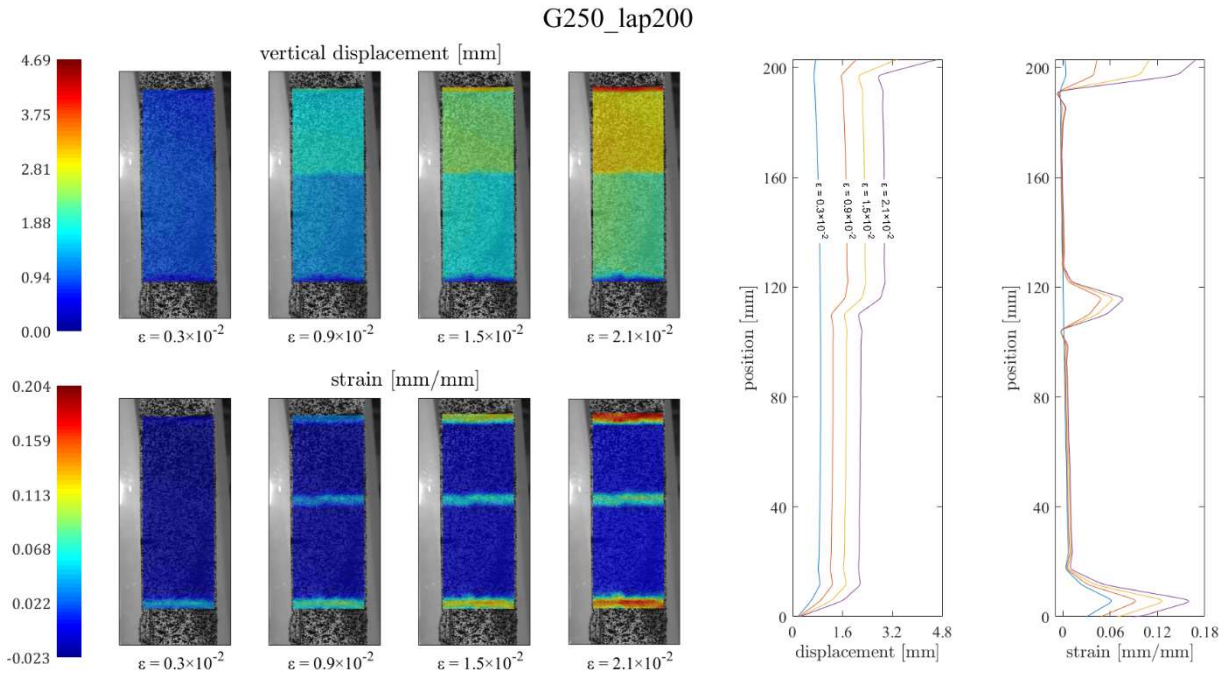

(d)

Fig. 8 – Evolution of the strain field during tensile tests on glass FRCM specimens, acquired with DIC, for different lengths of fabric overlapping.

4.2 Failure modes

Different failure modes have been observed depending on the configuration of the glass fabric reinforcement. FRCM specimens reinforced with a continuous layer of fabric failed after the formation of two or three cracks within the mortar matrix. Usually, after the formation of cracks, one or two of them propagate and their opening increases up to reach the specimen failure. Even after the formation of cracks, the load carried by the specimen increases, until reaching the breakage of the yarns close to one of the cracks.

In the case of G250_Lap100, the formation of a longitudinal cracks is clearly observed at the interface between the fabrics' overlap (Fig. 9). This effect is caused by the slippage of the fabrics along the overlay interface, until the specimen is broken.

For longer overlap lengths (G250_lap150, G250_lap200), the formation of longitudinal cracks and the slippage between fabrics is prevented. The failure mode observed is similar to that of specimens with a single fabric layer. However, it can be observed that the cracks width of specimens with overlapped fabrics is smaller than that of specimens with single layer. The presence of a double layer of fabric limits the cracks opening by increasing the stiffness of the composite.

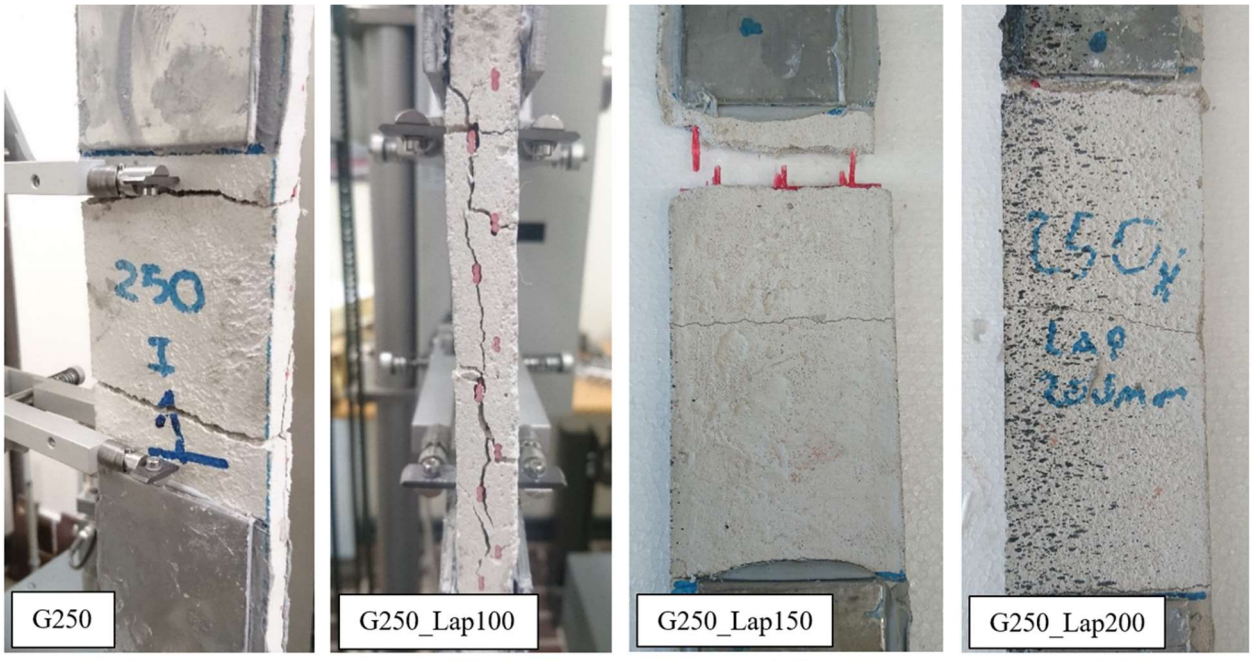

Fig. 9 – Failure modes of FRCM specimens: (a,c,d) fabric breakage, (b) slippage at the fabric-to-matrix interface

5. Variational Model

5.1 Model assumptions and governing equations

FRCM specimens are modeled as series of layers of mortar and reinforcement fabrics, connected to each other by elastic interfaces, as illustrated in the geometrical scheme of Fig. 10(a). The kinematical descriptors of each layer are the longitudinal displacement $u_i = u_i(x)$ and the damage parameter $\alpha_i = \alpha_i(x)$, with x the longitudinal coordinate, and the index i referring to the i-th layer. Damage α_i assumes values in the interval [0,1]: $\alpha_i=0$ means that the material is sound, and $\alpha_i=1$ means that it is completely broken. In the following, a prime will be used for derivative with respect to x, and a dot for derivation with respect to the evolution parameter t, called *time* for simplicity and introduced in the following.

To avoid damage healing, the irreversibility condition

$$\dot{\alpha}_i \geq 0 \tag{1}$$

is assumed.

For each layer of length $l+2\hat{l}$, with l the free length and $\hat{l}$ the anchor length, the internal energy is

$$\mathcal{E}_i(u_i,\alpha_i) = \int_0^{l+2\hat{l}} \left\{ \frac{1}{2}(1-\alpha_i)^2 A_i E_i u'^2_i + \frac{A_i}{E_i}\sigma^2_{e,i}\left(\alpha_i + \frac{l_i^2}{16}\alpha'^2_i \right) \right\} dx\,. \tag{2}$$

As usually assumed in phase-field approaches [38], the energy is sum of two terms: an elastic energy (first term of the integral), which is a quadratic function of the strain u_i', and a fracture energy (second term of the integral), which has a local contribution, linear with respect to α_i, and a non-local contribution, depending on the gradient of α_i. Geometrical and material parameters to be assigned within the energy (2) are the cross-section area A_i, the Young's modulus E_i, the maximum tensile stress $\sigma_{e,i}$ that material can sustain before breaking, and the size l_i of the process zone where damage localizes and coalesces into fracture.

Interfaces between adjacent layers are linearly elastic. The energy between the j-th and the (j+1)-th layer is

$$\mathcal{E}_{j,j+1}(u_j,u_{j+1}) = h\int_0^{l+2\hat{l}} \frac{1}{2}k_{j,j+1}(u_j-u_{j+1})^2\,dx\,, \tag{3}$$

where $k_{j,j+1}$ is the elastic coefficient, and h is the width of the interface. The total internal energy of the system is

$$\mathcal{E} = \sum_{i=1}^{N}\mathcal{E}_i(u_i,\alpha_i) + \sum_{j=1}^{N-1}\mathcal{E}_{j,j+1}(u_j,u_{j+1})\,, \tag{4}$$

where N=3 and N=4 in the cases of single ply and lap-spliced plies samples, respectively. The constitutive parameters E_i, $\sigma_{e,i}$ and l_i in (2), and $k_{j,j+1}$ in (3) are assumed constant at least in each part of the samples (central part or ending reinforced parts), according to the schemes drawn in Fig. 10(a,b) for the one ply specimen and the lap splice overlap specimen, respectively. Different colors are used in Fig. 10(a,b) to distinguish the different materials and interfaces. Parameters of the mortar layers are the Young's modulus E_m, the peak elastic stress $\sigma_{e,m}$ and the internal length l_m. The ending parts of the mortar layers are assumed to be unbreakable. The constitutive parameters of the fabric layers are E_f, $\sigma_{e,f}$ and l_f.

Three different interfaces are considered. The fabric-to-mortar interface is linearly elastic with elastic modulus k_{fm}. Indeed, according to [54], the shear stress leading to fabric slippage is larger than 1 MPa, value never attained in simulations. A bilinear shear stress-displacement law is

assumed for the fabric-to-fabric interface, as drawn in Fig. 11, where the softening branch account for debonding and slippage. Mortar-to-mortar interface, which is present in the geometrical scheme of the lap-spliced sample of Fig. 10(c), is supposed to be rigid to guarantee continuity among adjacent layers. Criterions to calibrate all the above-mentioned parameters and values used in simulations are given in the next Subsect. 5.2.

Longitudinal stresses σ_i in the layers and shear stresses $\tau_{j,j+1}$ at interfaces are obtained by differentiating (2) with respect to the strain u_i', and (3) with respect to the relative displacement $(u_j - u_{j+1})$ respectively,

$$\sigma_i = (1-\alpha_i)^2 E_i u_i'^2, \quad \tau_{j,j+1} = k_{j,j+1}(u_j - u_{j+1}). \tag{5}$$

In experiments, tensile displacement is imposed at the upper extremity of the specimen, where a clevis joint connects the sample to the testing frame. To reproduce this situation, the bottom ends of the mortar layers are fixed, and the displacement

$$u = t(l + 2\hat{l}), \tag{6}$$

is imposed at the upper ends (see Fig. 10(b,c)). The assigned deformation t is positive and increasing. It represents the evolution parameter, called *time* for brevity. Since the clevis-grip method allows for the slippage of the fabric from the inorganic matrix, boundaries of the fabric layers are left free to move.

Since external loads are not considered, and body loads (as weight loads) are neglected, the internal energy (4) coincides with the total energy of the system. By following a standard variational procedure, balance equations are obtained by requiring the first variation of energy (4) to be non-negative for any admissible perturbation, and they read

$$\begin{aligned} &\frac{A_i}{h}\sigma_i' - \tau_{i,i+1} + \tau_{i-1,i} = 0, \\ &(1-\alpha_i)A_i E_i u_i'^2 - \frac{h_i}{E_i}\sigma_{e,i}^2\left(1 - \frac{l_i^2}{16}\alpha_i''\right) \le 0, \quad i = 1,...N. \end{aligned} \tag{7}$$

The first equation is the i-th macroscopic balance equation, which is coupled with the (i-1)-th and (i+1)-th equations through the shear stresses $\tau_{i-1,i}$ and $\tau_{i,i+1}$. The second equation is the yielding condition for damage α_i, which has the form of an inequality because of the constrain (1). Using $(4)_1$, it rewrites

$$\sigma_i \le \sigma_{e,i}\sqrt{(1-\alpha_i)^3\left(1 - \frac{l_i^2}{16}\alpha_i''\right)} = \sigma_{y,i}(\alpha_i), \tag{8}$$

which states that the stress σ_i in the i-th layer can never exceed the yield stress $\sigma_{y,i}$, and, when it is equal to the yield stress, damage can develop.

In an evolution process of increasing stretching, starting from an initial unstretched state, the system experiences elastic deformation, which develops as long as $\sigma_i < \sigma_{y,i}(0) = \sigma_{e,i}$. When σ_i reaches the limit value $\sigma_{e,i}$, damage forms and coalesces into a fracture. Accordingly, $\sigma_{e,i}$ is the maximum elastic stress that the i-th layer can sustain before failure.

The evolution problem is formulated as a constrained quadratic programming problem solved at each time increment. Hereinafter, the problem is briefly presented, and the reader is referred to [48-50] for an in-depth description. Time t is discretized into finite intervals of size τ, and, within each time step $t \to t + \tau$, variables are approximated by the linear expressions

$$u_i(x,t+\tau)=u_i(x,t)+\tau\dot{u}_i(x,t),\qquad \alpha_i(x,t+\tau)=\alpha_i(x,t)+\tau\dot{\alpha}_i(x,t), \tag{9}$$

and the energy (4) is developed up to the second order, around the configuration at time t,

$$\mathcal{E}(t+\tau)=\mathcal{E}(t)+\tau\dot{\mathcal{E}}(t)+\frac{1}{2}\tau^2\ddot{\mathcal{E}}(t), \tag{10}$$

which can be rewritten as sum of a constant term and a quadratic functional of $\dot{u}_i$ and $\dot{\alpha}_i$ in the following form

$$\mathcal{E}(t+\tau)=\text{const}+\tau\mathcal{F}(\dot{u}_i,\dot{\alpha}_i),\quad i=1,...,N. \tag{11}$$

If $u_i(x,t)$ and $\alpha_i(x,t)$, i=1,…,N, are known at the instant t, the solution (9) at the instant $t+\tau$ is determined by (9), where the rates $\dot{u}_i$ and $\dot{\alpha}_i$ solve the constrained programming problem

$$(\dot{u}_i,\dot{\alpha}_i)=\arg\min\left\{\mathcal{F}(\dot{u}_i,\dot{\alpha}_i),\quad \dot{\alpha}_i\geq 0,\quad i=1,...,N,\quad +b.c.\right\} \tag{12}$$

This minimum problem is numerically solved by means of a finite element code which implements an alternate iterative minimization procedure, consisting in minimizing the energy functional with respect to the unknown fields separately.

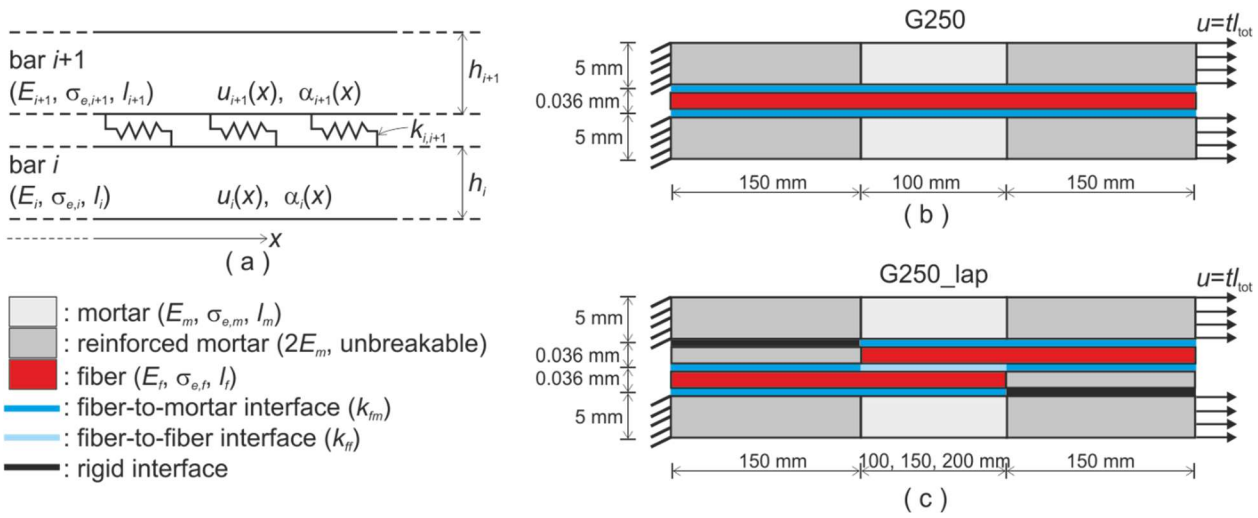

Fig. 10 – Geometrical schemes: (a) generic multilayer beam, (b) sample with a single fabric reinforcement layer, (c) sample with two overlapped layers.

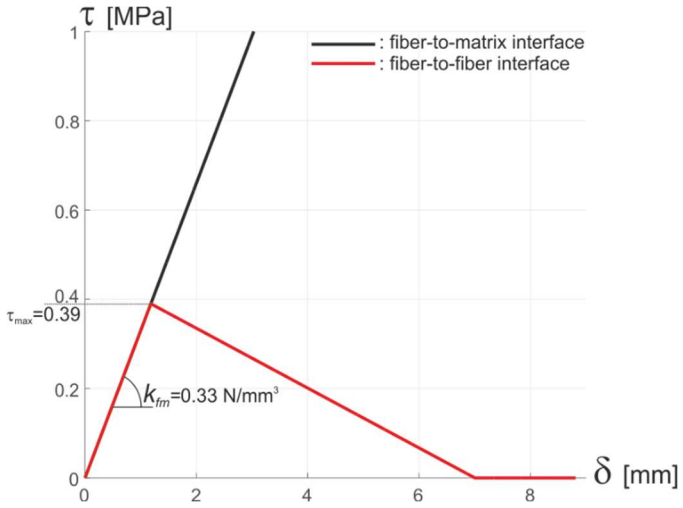

Fig. 11 Constitutive laws of fiber-to-matrix and fiber-to-fiber interfaces.

5.2 Parameters calibration and setting

Specimens geometrical schemes are drawn in Fig. 10. The anchor length is $\hat{l}=150$ mm. For the one ply specimen (G250), the free length is l=100 mm, and, for the lap-spliced samples, three different lengths l=100, 150 and 200 mm are considered. The thickness of mortar layers is 5 mm, and the thickness of fabric layer is 0.04 mm, which is obtained by distributing the cross-section area of the fabric (A_f=2.77 mm^2, corresponding to the cross-section areas of three yarns) through the layer width h=70 mm.

Concerning the constitutive parameters, Young's moduli of Glass 250 fabric and mortar are given in Table 1, and they are E_f=57.1 GPa, and E_m=9.5 GPa, respectively. Also the yarns peak stress $\sigma_{e,f}$=1405 MPa is reported in Table 1. The matrix ultimate tensile stress $\sigma_{e,m}$=2.4 MPa is the average stress that leads to the opening of the first crack in the matrix recorded during tensile tests on one-ply specimens. Values of internal lengths are l_m=0.6 mm, as acquired with DIC, and l_f=0.1 mm.

The elastic coefficient of yarn-to-matrix interface has been estimated in [54], where the value k=3.10 MPa has been found. Since the interface area per unit length of the fabric is 15 mm^2 (three longitudinal yarns are considered), and the multilayer geometrical scheme of the model accounts for an interface area per unit length equal to 140 mm^2, the equivalent elastic coefficient is $k_{fm} = (15/140)k = 0.33$ MPa.

A piecewise linear law has been chosen for the fiber-to-fiber interface, as shown in Fig. 11, the slope of the first increasing branch is k_{fm}. The value of the maximum shear stress is τ_{max}=0.39 MPa, which allows to reproduce failure by slippage and failure by fabric breakage when the lap splice overlap is 100 and 150 mm, respectively, as found in experiments. The slope of the softening branch has been fixed by curve fitting.

6. Numerical results

Numerical stress-strain curves are compared to the experimental curves in Fig.7. Numerical curves accurately fit the experimental ones. Only in cases of G250_Lap150 and G250_Lap200, strains are slightly overestimated. Each stress drop of the numerical curves corresponds to the

opening of a fracture. Failure by reinforcement breakage is observed in specimens G250, G250_Lap150 and G250_Lap200. In these cases, fabric failure leads to brutal stress drop to zero. Failure by interface slippage is registered in G250_Lap100, and the slippage process is associated to the softening branch of Fig. 7(b).

The tensile test of G250 sample is simulated for first. Fig. 12 shows profiles of u and σ at different strains ε in the central part of the upper and lower mortar layers. Initially, the stretching process is linearly elastic, and stresses homogeneously grow in the layers. When the stress on the mortar reaches the peak limit value $\sigma_{e,m}$, two cracks form simultaneously, one in each mortar layer. In simulations, the value $\sigma_{e,m}$=2.4 MPa is perturbed with a random function of amplitude equal to 2% of $\sigma_{e,m}$. Looking to Fig. 12(a,c), where cracks correspond to displacement jumps, the first two cracks forms at x=26 mm in the upper layer and x=90 mm in the lower one. Their openings correspond to the first jump of the response curve of Fig. 7(a). From this point on, displacements and stresses evolve according to the solid line profiles of Fig. 12. Notice that stresses nullify at crack, and they progressively increase away from it. At $\varepsilon = 1 \cdot 10^{-2}$, σ reaches $\sigma_{e,m}$ at the left endpoint of the lower layer, and, consequently, a crack opens there. It corresponds to the second drop of the stress-strain curve. In the upper layer, the second fracture forms later, at $\varepsilon = 1.6 \cdot 10^{-2}$, when the peak stress is reached at the right endpoint (third drop of the stress-strain curve). Dashed profiles in Fig. 12 refer to the evolution with two cracks in each mortar layer. Profiles of σ in the reinforcement layer are plotted in Fig. 13 for different values of the imposed strain ε. In those points where mortar layers are cracked, stresses attain the maximum values, because of stresses transfer from the matrix to the reinforcement. At $\varepsilon = 4.6 \cdot 10^{-2}$, the yield stress $\sigma_{e,f}$=1405 MPa is attained on the right side of the reinforcement layer, close to the right endpoint, where both the upper and lower mortar layers are fractured. At this point the fabric layer breaks and a passing crack leads the sample to failure. Damage fields α_i in each layer at the final failure stage are plotted in Fig. 14, using different colors. Numbers indicate the sequence of cracks opening in the evolution process. A sketch of the broken sample is also drawn in Fig. 14.

Finally, notice the large similarity between the profiles of u of Fig. 8(a) and the displacement evolution in the lower layer found by simulations, plotted in Fig. 12c. In both the cases, a first crack opens in a point close to the right endpoint, and, later, a second crack forms at the left endpoint. This sequence of two cracks formation in the mortar layer, the first in an arbitrary point, often close to one endpoint, and the second at the most distant endpoint from the first crack, has been observed in experiments and found in simulations.

Results of tensile tests on lap-spliced specimens are described in Figs. 15 and 16. First, the overlap length l=100 mm is considered. Fig. 15 shows the displacement profiles in the four layers of the specimen at instants which correspond to the opening of cracks and to the final interfacial slippage. Initially, two cracks open simultaneously in the mortar layers in correspondence of the fabrics' extremities, where strength is reduced by the pre-cracks introduced to separate fabrics from mortar (Fig. 15a). The opening of these fractures corresponds to the first deep drop of the stress-strain curve of Fig. 7b. The next two fractures open in the mortar layers at sides opposite to those of the first two cracks. They form at different instants, first in the upper layer (Fig. 15b) and then in the lower one (Fig. 15c), corresponding to the second and third drops of the response curve. At this point, stresses are basically transferred from one side of the sample to the other by the two overlapped

reinforcements and thus large amount of shear stresses develop at the interface between them. When the shear stress reaches the maximum value τ_{max} (see Fig. 11), then slippage initiates and evolves. This phase corresponds to the softening branch of the response curve. The slipping displacement δ at the end of the slippage stage is reported in Fig. 15d.

Notice that cracks open at the extremities of the specimens also in experiments. An example is shown in Fig. 8(b), where displacement profiles given by DIC are plotted at different strains. In this case, the first fracture forms on the right side, and the second one opens close to the left boundary.

In case of larger overlap lengths (l=150, 200 mm), shear stresses distribute on larger interface surfaces and thus smaller values of τ are attained. As a result, slippage does not activate, and failure occurs by fabric breaking. Fig. 16a shows the displacement profiles of the four layers of the system right before failure, when the overlapping length l=150 mm is chosen. Even now, four cracks forms in the mortar at the boundaries of the specimen free area, two in each side (Fig. 16c). Stresses in the two fabrics before failure are plotted in Fig. 16b. They decrease going toward the ending sections. In the right side of the upper fabric, the fracture stress $\sigma_{e,f}$=1405 MPa is approached, and, as a result, a crack forms therein, leading the specimen to failure (Fig. 16d). In this case, the limit shear stress τ_{max} is never reached at the interface between fabrics, and, accordingly, slippage does not activate.

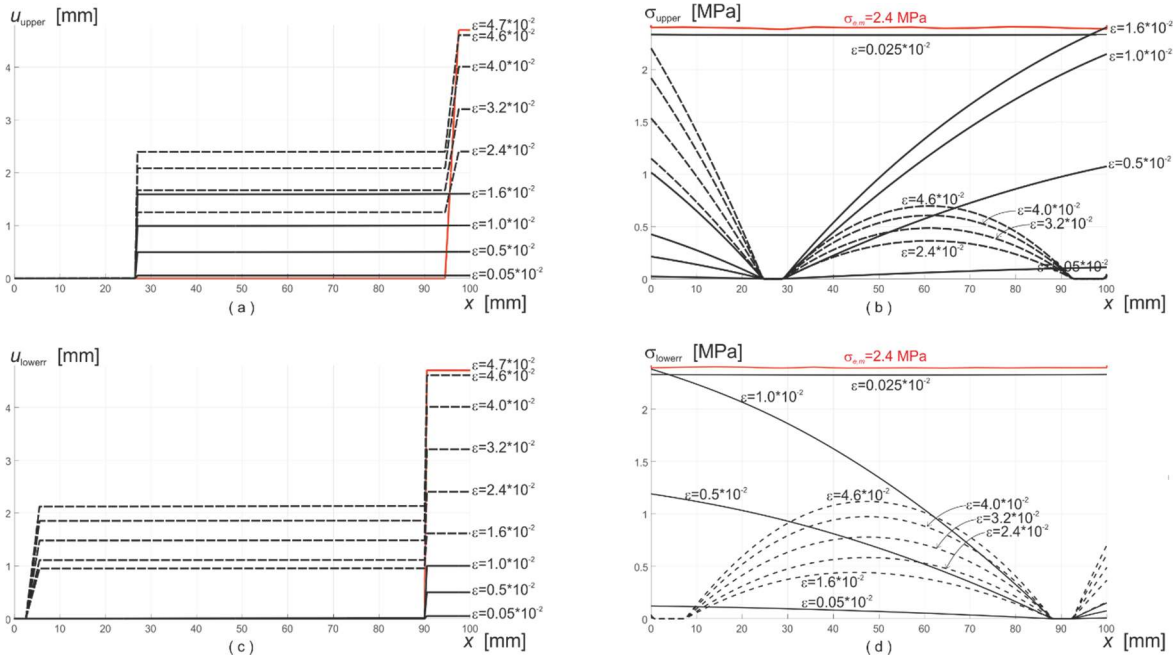

Fig. 12 – Specimen with a single fabric reinforcement layer. Profiles of u at different strains ε in the upper (a) and lower (c) mortar layers; profiles of stress σ in the upper (b) and lower (d) mortar layers.

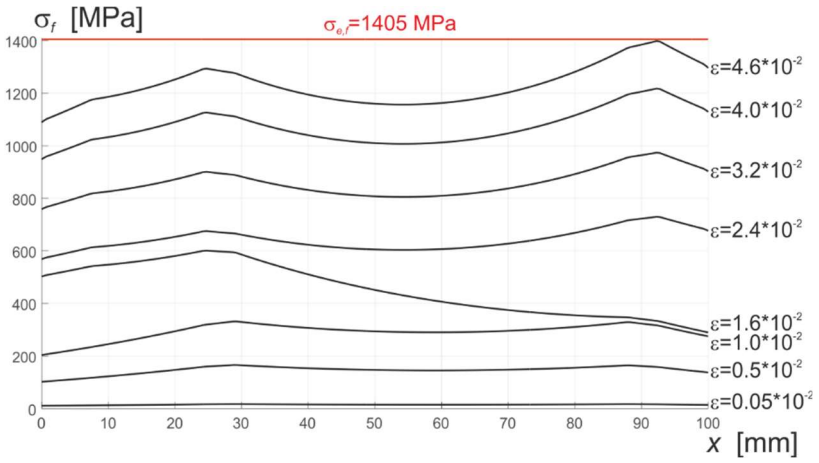

Fig. 13 – Specimen with a single fabric reinforcement layer. Profiles of stress σ at different strains ε in the fiber reinforcement layer.

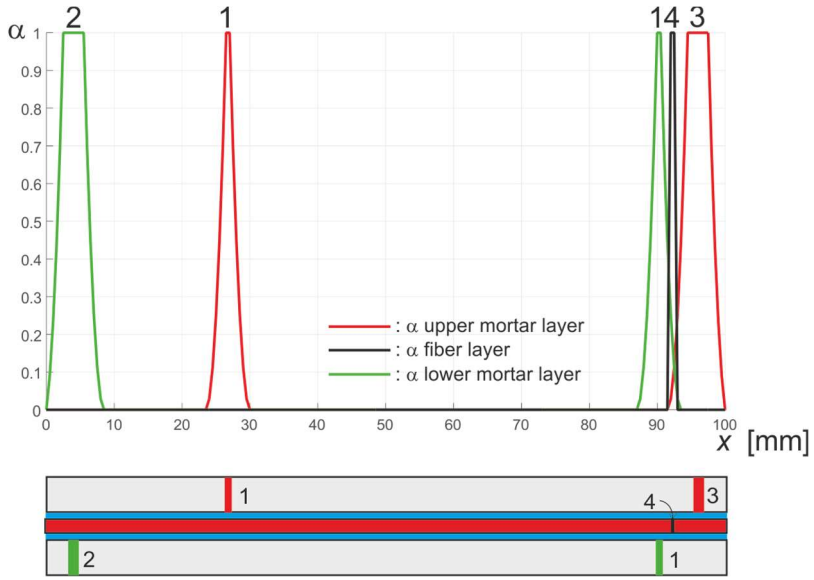

Fig. 14 – Specimen with a single fabric reinforcement layer. Damage fields in the different layers at failure. Numbers refer to the sequence of crack opening.

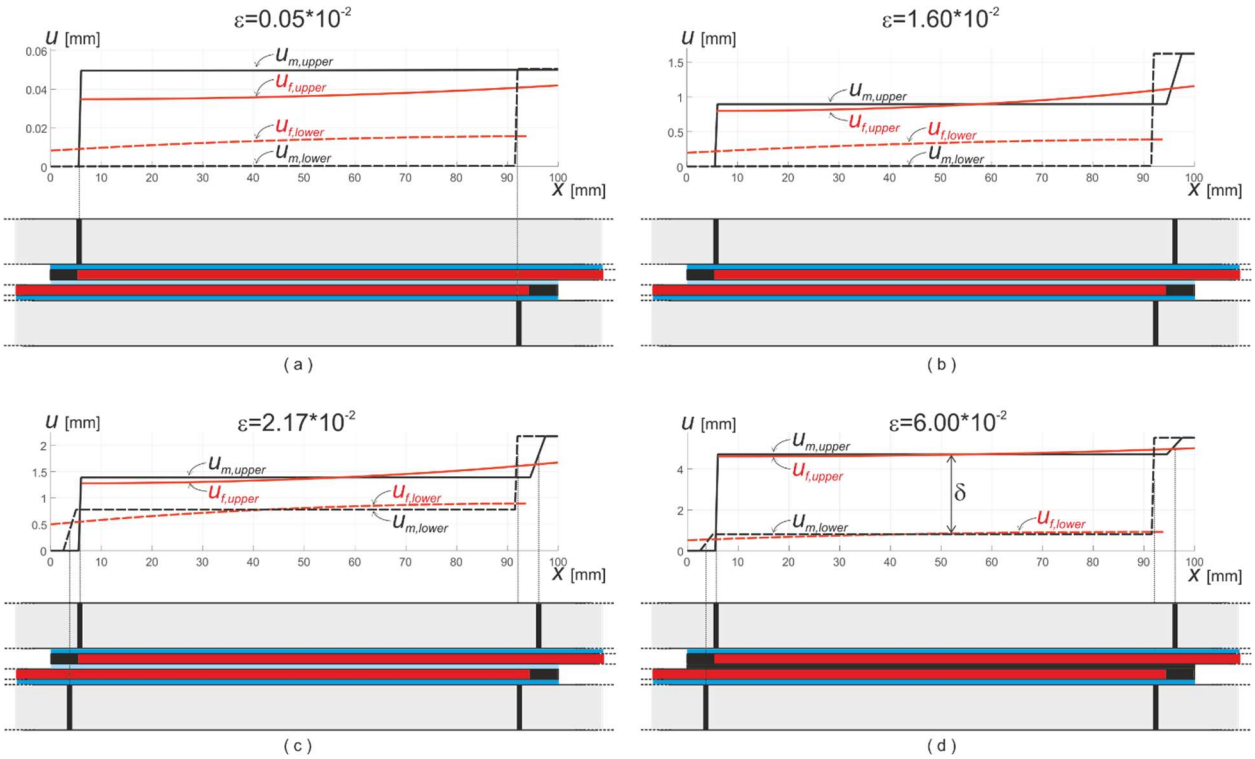

Fig. 15 – Specimen with overlapped fabric layers with lap splice overlap of 100 mm. Profiles of u in the four layers at different strains ε, and sketches of fracture positions in the multilayer system.

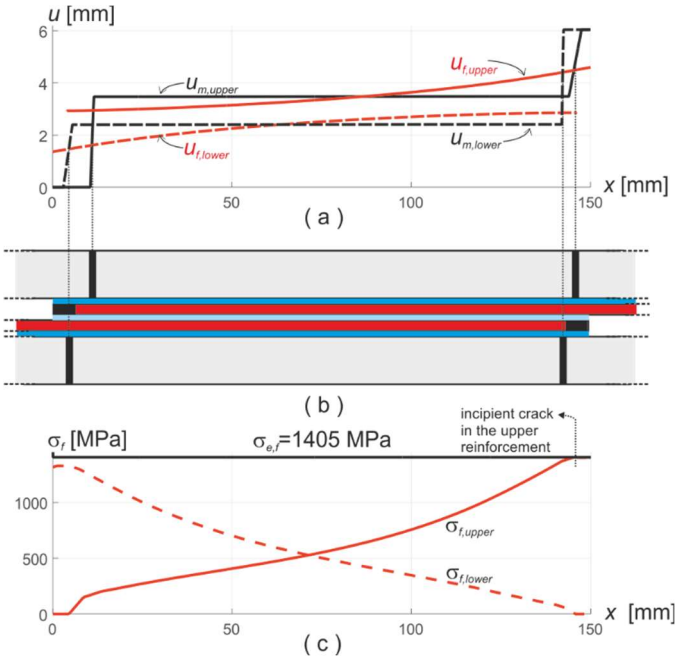

Fig. 16 – Specimen with overlapped fabric layers with lap splice overlap of 150 mm. Profiles of u in the four layers (a), cracks positions in the specimen (b), and profiles of σ in the reinforcement layers (b) at ε=0.04, before failure.

7. Conclusions

Tensile characterization of FRCM specimens with continuous and overlapped glass fabrics has been carried out by using a clevis type gripping method. Deformations and failure modes of FRCM specimens have been deeply investigated by means of DIC and compared with numerical simulations.

- Different failure modes have been observed in tensile tests, depending on the overlap length. Specimens reinforced with a single layer of glass fabric failed due to fabric rupture within the free length of the specimen, after the formation of two or three cracks. FRCM specimens with fabrics' overlap length of 100 mm failed due to slippage at the overlay interface. Increasing the overlap length to 150 and 200 mm led to the breakage of one of the glass fabric layers.
- The minimum glass fabrics' overlap length, which allows to restore the specimen's integrity and the complete transfer of tensile stresses from one fabric to another, is about 150 mm. With this overlap length, the maximum stress attained at failure is almost the same of that of specimens with continuous fabric, while the stiffness is greatly increased. In case of smaller overlap lengths, the maximum tensile stress to which the fabric is subjected is much lower and the failure occurs at the interface between the two layers of fabrics.
- DIC was able to provide important information about the mechanical behaviour of FRCM specimens during tensile tests. It allowed to detect the number and width of the cracks at any load value and the strain field on the whole surface of the specimen.
- A variational model has been developed to provide a thorough understanding of failure mechanisms of the different FRCM systems, subjected to tensile loads. Specimens have been schematized as a sequence of one-dimensional brittle bars, coupled by non-linear elastic connections. Different stiffnesses and strengths were given to the central and side parts of the mortar bars to take into account the clevis type anchoring system, and different constitutive laws were assigned to fiber-to-matrix and fiber-to-fiber interfaces to simulate the FRCM behaviour with continuous and overlapped fabrics. The evolution problem, formulated as an incremental constrained minimum problem, has been implemented in a finite element code.
- The model, despite its simplicity, has accurately captured all the evolution stages leading to specimens' failure modes that have been observed in experiments. The evolution of crack patterning in the mortar layers has been carefully described, and the two different mechanisms of failure, breakage of the reinforcement and slippage at fiber-to-fiber interface, have been reproduced. Finally, the stress-strain curves obtained from simulations have been compared with the experimental ones providing a great predictive capability.

Data availability

The raw/processed data required to reproduce these findings cannot be shared at this time as the data also forms part of an ongoing study

References

[1] Papanicolaou CG, Triantafillou TC, Papathanasiou M, Karlos K. Textile reinforced mortar (TRM) versus FRP as strengthening material of URM walls: out-of-plane cyclic loading. *Materials and Structures,* 2008; 41: 143-157.

[2] Nanni A. FRCM strengthening e a new tool in the concrete and masonry repair toolbox. *Concrete International*, 2012; 34(4): 43-49.

[3] Corinaldesi V, Donnini J, Mazzoni G, Experimental study of adhesion between FRCM and masonry support. *Key Engineering Materials*, 2015; 624: 189-196.

[4] De Felice G, De Santis S, Garmendia L, Ghiassi B, Larrinaga P, Lourenco PB, Oliveira DV, Paolacci F, Papanicolaou CG. Mortar-based systems for externally bonded strengthening of masonry. *Materials and Structures*. 2014; 47: 2021–2037.

[5] Raoof SM, Koutas LN, Bournas DA. Textile-reinforced mortar (TRM) versus fibre-reinforced polymers (FRP) in flexural strengthening of RC beams. *Construction and Building Materials*. 2017; 151: 279–291.

[6] Escrig C, Gil L, Bernat-Maso E. Experimental comparison of reinforced concrete beams strengthened against bending with different types of cementitious-matrix composite materials. *Construction and Building Materials.* 2017; 137: 317-329.

[7] Aljazaeri ZR, Myers JJ. Strengthening of reinforced-concrete beams in shear with a fabric-reinforced cementitious matrix. *Journal of Composites for Construction*. 2017; 21(5): 1–11.

[8] Pellegrino C, D'Antino T. Experimental behaviour of existing precast prestressed reinforced concrete elements strengthened with cementitious composites. *Composites Part B: Engineering*, 2013; 55: 31–40.

[9] Triantafillou TC, Papanicolaou CG. Shear strengthening of reinforced concrete members with textile reinforced mortar (TRM) jackets. *Materials and Structures*, 2006; 39(1): 93–103.

[10] Younis A, Ebead U, Shrestha KC. Different FRCM systems for shear strengthening of reinforced concrete beams. *Construction and Building Materials.* 2017; 153: 514–526.

[11] Loreto G, Babaeidarabad S, Leardini L, Nanni A. RC beams shear-strengthened with fabric-reinforced-cementitious-matrix (FRCM) composite. *International Journal of Advanced Structural Engineering,* 2015; 7(4): 341-352.

[12] Ombres L. Debonding analysis of reinforced concrete beams strengthened with fiber reinforced cementitious mortar. *Engineering Fracture Mechanics*, 2012; 81: 94-109.

[13] Trapko T. Effect of eccentric compression loading on the strains of FRCM confined concrete columns. *Construction and Building Materials*, 2014; 61: 97-105.

[14] Triantafillou TC, Papanicolaou CG, Zissimopoulos P, Laourdekis T. Concrete confinement with textile reinforced mortar (TRM) jackets. *ACI Struct. J*. 2006; 103(1): 28–37.

[15] Ombres L, Verre S. Structural behaviour of Fabric Reinforced Cementitious Matrix (FRCM) strengthened concrete columns under eccentric loading. *Composites Part B: Engineering*, 2015; 75: 235-249.
[16] De Caso y Basalo FJ, Matta F, Nanni A. Fiber reinforced cement-based composite system for concrete confinement. *Construction and Building Materials*. 2012; 32: 55–65.
[17] Colajanni P, De Domenico F, Recupero A, Spinella N. Concrete columns confined with fibre reinforced cementitious mortars: Experimentation and modelling. *Construction and Building Materials*, 2014; 52: 375-384.
[18] Alecci V, Misseri G, Rovero L, Stipo G, De Stefano M, Feo L, Luciano R. Experimental investigation on masonry arches strengthened with PBO-FRCM composite. *Composites Part B: Engineering*, 2016; 100: 228-239.
[19] Babaeidarabad S, De Caso y Basalo F, Nanni A. URM Walls Strengthened with Fabric-Reinforced Cementitious Matrix Composite Subjected to Diagonal Compression. *Journal of Composites for Construction*, 2013; 18(2).
[20] Babaeidarabad S, De Caso y Basalo F, Nanni A. Out-of-Plane behavior of URM Walls Strengthened with Fabric-Reinforced Cementitious Matrix Composite. *Journal of Composites for Construction,* 2013; 18(4).
[21] Babaeidarabad S, Arboleda D, Loreto G, Nanni A. Shear strengthening of un-reinforced concrete masonry walls with fabric-reinforced-cementitious-matrix. *Construction and Building Materials*, 2014; 65: 243-253.
[22] De Felice G, De Santis S, Garmendia L, Ghiassi B, Larrinaga P, Lourenço PB, Oliveira DV, Paolacci F, Papanicolaou CG. Mortar-based systems for externally bonded strengthening of masonry. *Materials and Structures* 2014; 47(12): 2021–2037.
[23] Alecci V, Focacci F, Rovero L, Stipo G, De Stefano M. Extrados strengthening of brick masonry arches with PBO–FRCM composites: Experimental and analytical investigations. *Composite Structures*, 2016; 149: 184-196.
[24] ACI 549.4 R-13. Guide to design and construction of externally bonded Fabric-Reinforced Cementitious Matrix (FRCM) systems for repair and strengthening concrete and masonry structures. Farmington Hills, MI: American Concrete Institute; 2013.
[25] AC 434-13. Acceptance criteria for masonry and concrete strengthening using fabric reinforced cementitious matrix (FRCM) composite systems; 2013.
[26] RILEM Technical Committee, 232-TDT (Wolfgang Brameshuber), Recommendation of RILEM TC 232-TDT: test methods and design of textile reinforced concrete – uniaxial tensile test: test method to determine the load bearing behavior of tensile specimens made of textile reinforced concrete, *Materials and Structures.* 2016; 49: 4923-4927.
[27] Arboleda D, Carozzi FG, Nanni A, Poggi C. Testing Procedures for the Uniaxial Tensile Characterization of Fabric-Reinforced Cementitious Matrix Composites. *Journal of Composites for Construction.* 2016; 20(3).
[28] D'Antino T, Papanicolaou CC. Comparison between different tensile test set-ups for the mechanical characterization of inorganic-matrix composites. *Construction and Building Materials*. 2018; 171: 140-151.
[29] Donnini J, Corinaldesi V. Mechanical characterization of different FRCM systems for structural reinforcement. *Construction and Building Materials*.2017; 145: 565-575.

[30] Caggegi C, Lanoye E, Djama K, Bassil A, Gabor A. Tensile behaviour of a basalt TRM strengthening system: Influence of mortar and reinforcing textile ratios. *Composites Part B*. 2017; 130: 90-102.
[31] Linea Guida per la identificazione, la qualificazione ed il controllo di accettazione di compositi fibrorinforzati a matrice inorganica (FRCM) da utilizzarsi per il consolidamento strutturale di costruzioni esistenti. Consiglio Superiore dei Lavori Publici – Servizio Tecnico Centrale. Luglio 2018.
[32] Badaloni M, Rossi M, Chiappini G, Lava P, Debruyne D. Impact of Experimental Uncertainties on the Identification of Mechanical Material Properties using DIC. *Experimental Mechanics*. 2015; 55: 1411-1426.
[33] Chiappini G, Sasso M, Bellezze T, Amodio D. Thermo-structural analysis of components in ceramic material. *Procedia Structural Integrity*. 2018; 8: 618-627.
[34] Sasso M, Chiappini G, Rossi M, Cortese L, Mancini E. Visco-Hyper-Pseudo-Elastic Characterization of a Fluoro-Silicone Rubber. *Experimental Mechanics*. 2014; 54(3): 315-328.
[35] Stazi F, Tittarelli F, Saltarelli F, Chiappini G, Morini A, Cerri G, Lenci S. Carbon nanofibers in polyurethane foams: Experimental evaluation of thermo-hygrometric and mechanical performance. *Polymer Testing*. 2018; 67: 234-245.
[36] Sasso M, Mancini E, Chiappini G, Sarasini F, Tirillò J. Application of DIC to Static and Dynamic Testing of Agglomerated Cork Material. *Experimental Mechanics*. 2018: 1-17.
[37] Tekieli M, De Santis S, De Felice G, Kwiecień A, Roscini F. Application of Digital Image Correlation to composite reinforcements. *Composite Structures*. 2017; 160: 670-688.
[38] Bilotta A, Ceroni F, Lignola GP, Prota A. Use of DIC technique for investigating the behaviour of FRCM materials for strengthening masonry elements. *Composites Part B*. 2017; 129: 251-270.
[39] Marigo JJ, Maurini C, Pham K. An overview of the modelling of fracture by gradient damage models. *Meccanica*. 2016; 51(12): 3107-3128.
[40] Bourdin B, Francfort GA, Marigo JJ. Numerical experiments in revisited brittle fracture. *J Mech Phys Solids.* 2000; 48(4): 797-826.
[41] Bourdin B, Francfort GA, Marigo JJ. The variational approach to fracture. *J Elast,* 2008; 91: 5-148.
[42] Lancioni G, Royer-Carfagni G. The variational approach to fracture mechanics. A practical application to the French Panthéon in Paris. *J Elast.* 2009; 95: 1-30.
[43] Amor H, Marigo JJ, Maurini C. Regularized formulation of the variational brittle fracture with unilateral contact: numerical experiments. *J Mech Phys Solids.* 2009; 57: 1209-29.
[44] Freddi F, Royer Carfagni G. Regularized variational theories of fracture: a unified approach. *J Mech Phys Solids.* 2010; 58: 1154-74.
[45] Alessi R, Ambati M, Gerasimov T, Vidoli S, De Lorenzis L. Comparison of Phase-Field Models of Fracture Coupled with Plasticity. *Advances in Computational Plasticity*. Ed. by E. Onate, D. Peric, E. de Souza Neto, and M. Chiumenti. 2018.
[46] Kumar A, Francfort GA, Lopez-Pamies O. Fracture and healing of elastomers: A phase-transition theory and numerical implementation. *J. of the Mechanics and Physics of Solids*. 2018; 112: 523-551.

[47] Wu T, Carpiu-Prisacari A, Poncelet M, De Lorenzis L. Phase-field simulation of interactive mixed-mode fracture tests on cement mortar with full-field displacement boundary conditions. *Engineering Fracture Mechanics*. 2017; 182: 658-688.
[48] Lancioni G, Corinaldesi V. Variational modelling of diffused and localized damage with applications to fiber-reinforced concretes. *Meccanica*. 2018; 53: 531–551.
[49] Del Piero G, Lancioni G, March R. A diffuse cohesive energy approach to fracture and plasticity: the one-dimensional case. *J Mech Mater. Struct*. 2013; 8 (2-4): 109-151.
[50] Lancioni G. Modeling the response of tensile steel bars by means of incremental energy minimization. *J Elast.* 2015; 121(1): 25-54.
[51] Lancioni G, Yalcinkaya T, Cocks A. Energy-based non-local plasticity models for deformation patterning, localization and fracture. *Proceedings of the royal society A*. 2015; 471.
[52] Alessi R, Marigo JJ, Vidoli S. Gradient damage models coupled with plasticity: variational formulation and main properties. *Mech. Mater*. 2015; 80: 351–367.
[53] Donnini J, De Caso y Basalo F, Corinaldesi V, Lancioni G, Nanni A. Fabric-reinforced cementitious matrix behavior at high-temperature: Experimental and numerical results. *Composites Part B.* 2017; 108: 108-121.
[54] Donnini J, Lancioni G, Corinaldesi V. Failure modes in FRCM systems with dry and pre-impregnated carbon yarns: Experiments and modelling, *Composites Part B*. 2018; 140: 57–67.
[55] Alessi R, Freddi F. Phase-field modelling of failure in hybrid laminates. *Composite Structures*. 2017; 181: 9–25.
[56] UNI EN 1015-11. Metodi di prova per malte per opere murarie - Determinazione della resistenza a flessione e a compressione della malta indurita; 2007.
[57] Amodio D, Broggiato G, Campana F, Newaz G. Digital Speckle Correlation for Strain Measurement by Image Analysis. *Experimental Mechanics*. 2003; 43(4): 396-402.